ChemComm
Chemical Communications

Accepted Manuscript

This article can be cited before page numbers have been issued, to do this please use: W. Gou and Y. Qu, *Chem. Commun.*, 2025, DOI: 10.1039/D5CC02887F.

ROYAL SOCIETY OF CHEMISTRY

rsc.li/chemcomm

View Article Online
DOI: 10.1039/D5CC02887F

ARTICLE

Electrospun nanofiber electrocatalysts: tailoring advanced architectures for oxygen evolution reaction

Received 00th January 20xx,
Accepted 00th January 20xx

DOI: 10.1039/x0xx00000x

Wangyan Gou[ab] and Yongquan Qu*[b]

Electrospinning technology has emerged as a pivotal platform for designing high-performance oxygen evolution reaction (OER) electrocatalysts, owing to its unparalled capability to fabricate nanostructures with tunable morphologies and compositions. This review systematically summarizes fundamental principles of electrospinning and recent advances in electrospun catalysts for OER, emphasizing structural engineering paradigms such as tubular, porous, hierarchical, composite, and high-entropy architectures. Despite compelling demonstrations of efficacy at laboratory scales, significant hurdles persist in achieving scalable manufacturing, cost efficiency, and long-term operational stability under industrial conditions. Future efforts should focus on developing low-cost precursors and high-throughput fabrication processes, employing *in situ*/*operando* characterization to unravel dynamic catalytic mechanisms, and optimizing device integration for practical applications. Electrospinning technology holds significant potential to deliver next-generation OER catalysts that combine efficiency, durability, and cost-effectiveness, accelerating their practical applications.

1. Introduction

Electrocatalysis plays a pivotal role in various energy conversion and storage systems, such as fuel cells, metal-air batteries, and water splitting.[1-6] Among these processes, oxygen evolution reaction (OER) is a fundamental half-reaction in various energy conversion and storage systems, such as water electrolysis for hydrogen production, metal-air batteries, and regenerative fuel cells. OER proceeds through distinct pathways dependent on the electrolyte environments: $H_2O \rightarrow O_2+4H^++4e^-$ in acidic electrolyte and $4HO^- \rightarrow O_2+2H_2O+4e^-$ in alkaline or neutral electrolyte.[7-9] Despite the indispensable roles of OER in sustainable energy technologies, its inherent four-electron process introduces sluggish reaction kinetics and high overpotentials, making it a major bottleneck that limits the operational efficiency of these electrochemical energy technologies.[10] To address the above challenges, the rational design of highly performed OER electrocatalysts have focused on the synergistic integration of maximizing accessible active sites, modulating the electronic structures of active site, tailoring the adsorption of oxygen-contained intermediates and accelerating charge/mass transport, thereby ensuring long-term operational stability of electrocatalysts.[11,12] The benchmark electrocatalyst for OER has been platinum group metals, particularly iridium oxide (IrO_2) and ruthenium oxide (RuO_2).[13,14] However, the high cost and unsatisfactory performance of these metals pose significant challenges for large-scale commercialization.[15] Consequently, extensive research efforts have been directed towards reducing usage, improving performance and exploring alternative materials.[16-18] In recent years, significant advancements have been made in the design and synthesis of efficient OER electrocatalysts. Key strategies include the development of heterostructures, hierarchical nanostructures, alloying, compositing with conductive supports, and engineering defect sites within the material.[19-23]

Electrospinning has emerged as a powerful and versatile platform for fabricating nanofibers (NF) with precisely controlled dimensions (nanometer to micrometer scale), tailored compositions, spanning polymers, ceramics, and functional composites.[24,25] By applying high-voltage electric fields to draw fibers from polymer solutions or melts, this technique enables the continuous production of one-dimensional (1D) nanostructures with programmable morphologies and architectures.[26] Therefore, electrospun nanofiber electrocatalysts, characterized by ultrahigh surface-area-to-volume ratios, hierarchically engineered porosity, modulated surface electronic configurations, and optimized mass/charge transport pathways, demonstrate remarkable enhancement of OER kinetics.[27,28] These synergistic structural attributes maximize the exposure of surficial active sites, accelerate electrolyte penetration and ion diffusion kinetics, and precisely tune the electronic configurations of active centers to achieve optimal adsorption energies for oxygen-containing intermediates, thereby substantially reducing overpotential requirements and elevating overall electrocatalytic efficiency. The growing academic and industrial adoption of electrospinning stems from its unique capability to engineer fiber properties through systematic

[a] School of Materials Engineering, Xihang University, Xi'an, 710077, China.
[b] Key Laboratory of Special Functional and Smart Polymer Materials of Ministry of Industry and Information Technology, School of Chemistry and Chemical Engineering, Northwestern Polytechnical University, Xi'an, 710072, China.

View Article Online
DOI: 10.1039/D5CC02887F

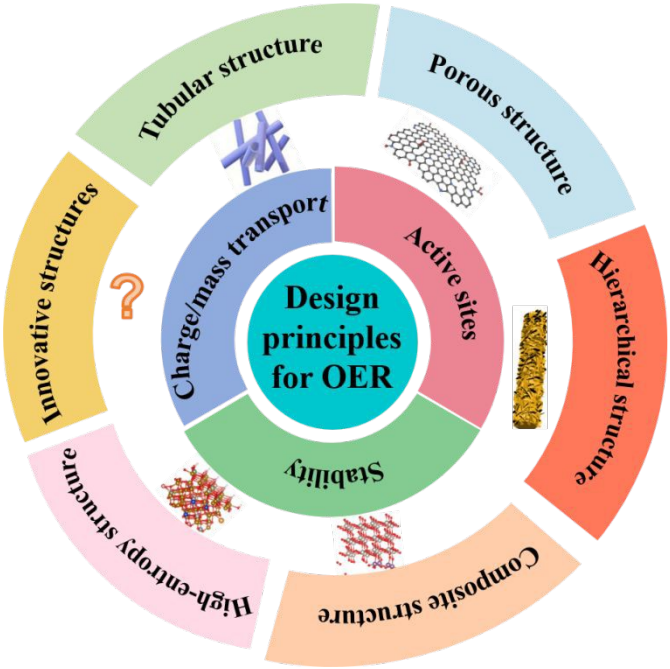

Fig. 1. Electrospinning technology for electrochemical OER.

optimization of three critical parameter classes: (1) solution properties (concentration, viscosity, conductivity, surface tension), (2) processing conditions (applied voltage, flow rate, collector distance), and (3) environmental factors (temperature, humidity).[29] The exceptional attributes of electrospun nanofibers, including high specific surface area, tunable porosity, and morphological versatility, have established them as ideal scaffolds for advanced electrocatalysis.[30] Recent breakthroughs in electrospinning methodologies have further expanded the design space, enabling the fabrication of sophisticated nanostructures (e.g., core-shell, hierarchical, and high-entropy architectures) that significantly enhance OER performance.[31-33] These developments demonstrate electrospinning's transformative potential in creating next-generation electrocatalytic materials with precisely engineered active sites and optimized mass/charge transport properties.

This feature article comprehensively examines our recent advances in designing Ir- and Ru-based electrocatalysts with tailored tubular and composite architectures for the enhanced OER performance. Notably, we have thoroughly and precisely elucidated the catalytic mechanism of these catalysts. Our work also highlights innovative design strategies leveraging electrospinning technology, which enables precise control over catalyst morphology and composition. The discussion begins with fundamental principles of electrospinning and progresses to examine various nanofiber architectures, including their synthesis-structure-property relationships. Special focus is given to breakthrough developments in composite, porous, hierarchical, and high-entropy nanofiber catalysts, highlighting their superior OER activity and stability, as shown in Fig. 1. Finally, we critically analyze remaining challenges and future opportunities in the rational design of electrospun OER catalysts, providing perspectives for both fundamental research and practical applications.

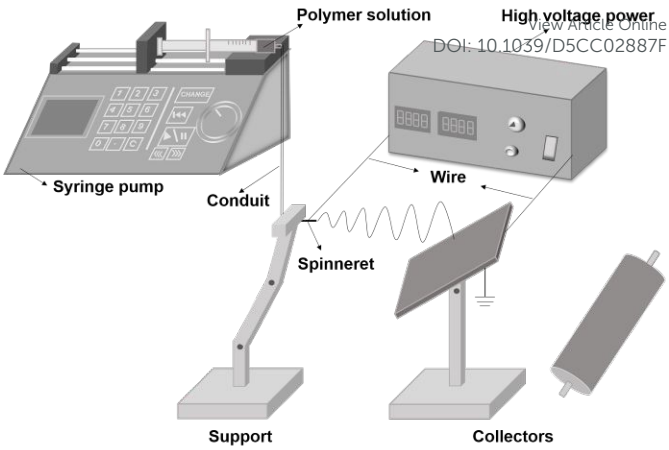

Fig. 2. Schematic illustration of electrospinning system.

2. Fundamentals of electrospinning

Since its emergence in the early 1990s, electrospinning technology has undergone significant advancements in both fundamental understanding and practical control of nanofiber formation.[34,35] This technique offers distinct advantages over alternative nanofiber production methods such as gas-jet spinning and melt fibrillation, particularly in terms of cost-effectiveness and scalability. A typical electrospinning setup comprises four essential components: (1) a high voltage power supply generating direct high current voltage; (2) a precision syringe pump with programmable flow control for delivery of the precursor solution; (3) a capillary spinneret to form Taylor cone through surface tension-electrostatic force balance; and (4) a conductive collector to establish a high-voltage electric field and to enable the fiber deposition (Fig. 2).

2.1 Solution preparation

This section systematically examines the critical parameters governing electrospinning outcomes, including solution properties, process conditions, and environmental factors, and their collective influence on the resulting nanofiber characteristics. Polymers and/or ionizable salts are dissolved in suitable solvents to form solutions with optimized concentration, viscosity, conductivity, and surface tension. Higher solution concentrations and viscosities yield thicker fibers, whereas excessively low values may cause fiber breakage or beading.[36] The electrical conductivity of the solution critically influences its rheological behavior and spinnability, primarily governed by the choice of polymers, solvents, and added salts. While higher conductivity promotes thinner nanofibers with enhanced bending instability and rapid solidification, excessive conductivity can destabilize the Taylor cone, leading to bead formation or irregular fiber nets.[37,38] Similarly, surface tension plays a key role: reducing it (e.g., via surfactants) facilitates uniform nano-net formation, but surpassing an optimal surfactant concentration induces defects due to colloidal aggregation from self-assembly.[39,40]

Polymers are commonly categorized by solvent compatibility for electrospinning applications.[41] Hydrophobic

polymers including polyacrylonitrile (PAN), polystyrene (PS), polyimide (PI), and polylactic acid (PLA) require organic solvents such as dimethylformamide (DMF), dimethyl sulfoxide (DMSO), and trichloroacetic acid (TCA). While these solvents offer excellent dissolution capacity, solution stability, and processing flexibility, they present significant environmental concerns, health hazards, and higher costs. Conversely, hydrophilic polymers like polyvinylpyrrolidone (PVP), polyvinyl alcohol (PVA) and chitosan are water-soluble. Although aqueous solutions provide distinct advantages in terms of environmental safety, cost-effectiveness, and biocompatibility, they exhibit poorer volatility control and solution stability, necessitating stricter regulation of polymer concentrations during processing.

2.2 Process conditions

The structural and morphological properties of electrospun nanofibers are predominantly controlled by three fundamental processing parameters: applied voltage, working distance, and solution flow rate.[42,43] The electric field strength requires precise optimization-while increased voltage promotes greater fiber stretching and diameter reduction, excessive voltages may cause electrical discharge or fiber discontinuity. Working distance presents a critical trade-off: insufficient distance prevents complete solvent evaporation, potentially causing fiber coalescence, while excessive distance leads to fiber instability and bead formation. Solution flow rate demonstrates a direct relationship with fiber diameter, as elevated feed rates increase mass deposition, consistently yielding thicker fibers. These parameters collectively determine the balance between fiber uniformity, morphology, and collection efficiency.

2.3 Environmental factors

Beyond the core processing parameters, ambient temperature and humidity significantly influence nanofiber morphology.[44,45] Elevated temperatures produce nanofibers with smoother surfaces and reduced diameters due to decreased solution surface tension and viscosity. However, accelerated solvent evaporation at higher temperatures can prematurely solidify fibers, terminating the electrically-driven stretching process. This dual effect necessitates careful temperature optimization, particularly for temperature-sensitive polymers where further investigation is required. Humidity similarly plays a critical role in fiber formation. Lower humidity conditions typically yield thinner fibers with fewer adhesive structures compared to those produced in more humid environments. These environmental factors interact complexly with solution properties and processing parameters to determine final fiber characteristics.

2.4 Spinneret and collector

To unlock the full potential of electrospun fiber architectures, innovative modifications to spinneret and collector designs have enabled the creation of diverse nanostructures with tailored morphologies.[46-48] These engineering advances have yielded three principal fiber configurations: randomly oriented mats, uniaxially aligned arrays, and coaxial core-shell structures, each maybe offering distinct advantages for electrocatalytic applications.

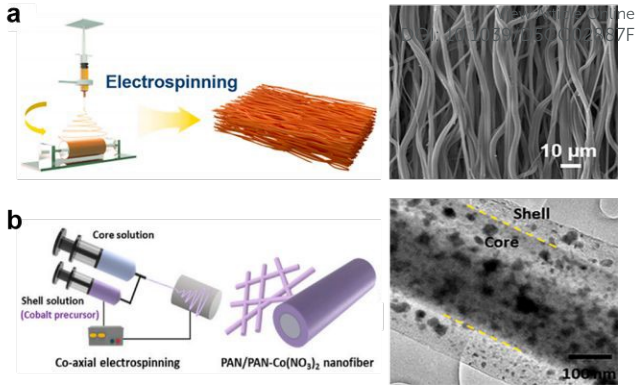

Fig. 3. (a) Preparation process and surface scanning electron microscope (SEM) image of aligned thermoplastic polyurethane (TPU) fibrous mat. Reproduced from ref. 53 with permission from Elsevier, copyright 2022. (b) Schematic of the preparation process of PAN/PAN-$Co(NO_3)_2$ and SEM image of the Co- CSNFs. Reproduced from ref. 56 with permission from Elsevier, copyright 2024.

2.4.1 Stationary collector. The basic electrospinning configuration, consisting of a single nozzle and a stationary metal plate or graphite paper collector, typically produces randomly oriented, non-woven fiber mats due to the chaotic whipping motion of fibers during deposition.[49,50] In this standard setup, the spinneret serves as the positive electrode while the collector functions as the negative electrode, with flexible positioning options (vertical or horizontal). Combining slow collector rotation with lateral nozzle movement can ensure even fiber distribution. Moreover, utilizing multi-nozzle arrays significantly increase production throughput while maintaining consistent fiber morphology. The Cr incorporated IrO_x nanofibers were synthesized via electrospinning using a precursor solution containing $Cr(CH_3COO)_3{\cdot}6H_2O$, $IrCl_3{\cdot}3H_2O$, PVP (M_W=1,300,000) in DMF.[51] The electrospinning process was performed with a single-nozzle configuration and aluminum foil collector, applying an electric field of 13 kV at a 15 cm working distance. Subsequent calcination in air yielded an oxide solid solution powder with rutile-phase structure comprising IrO_2 and CrO_2. Transmission electron microscopy (TEM) analysis revealed the resulting $Ir_{0.6}Cr_{0.4}O_x$-350 catalyst exhibited a unique nanowire morphology with an average diameter of ~50 nm. These randomly oriented nanowires consisted of ~2 nm nanocrystalline domains, creating a characteristically rough surface texture. X-ray diffraction (XRD) and elemental mapping from energy dispersive spectroscopy (EDS) confirmed the successful solid solution formation and homogeneous distribution of Ir, Cr, and O throughout the nanowire structure.

2.4.2 High-speed rotating collector. Aligned fiber architectures demonstrate superior performance in applications ranging from carbon fiber-reinforced nanocomposites to neural tissue engineering. The electrospinning process inherently induces macromolecular chain orientation along the fiber axis due to intense elongational strains and shear forces within the electrified jet, yielding mechanically enhanced fibers compared to their isotropic counterparts.[52,53] The predominant method for producing aligned fibers employs high-speed rotating collectors (drums or

disks). During deposition, fibers become electrostatically anchored to the rotating surface, which applies continuous tensile forces to the whipping jet. This mechanical drawing effect improves with rotational speed, enhancing fiber alignment. However, excessive rotational velocities can lead to fiber breakage, necessitating careful optimization of collector speed relative to solution properties and processing parameters. Zeng et al. demonstrated the fabrication of aligned PAN nanofibers through high-speed electrospinning, employing distinct parameters for different precursor solutions. The 10 wt % PAN solution in DMF need an applied positive voltage of 18 kV, a rate of 2000 rpm, and a distance of 15 cm between the needle tip and the collector to form well-aligned nanofiber onto a drum collector.[54] Another electrospinning solution was prepared by dissolving 12 wt% PAN powder in DMF solution, whose aligned nanofiber was obtained by a speed of 1500 rpm and a voltage of 20 kV with maintaining the same working distance. The aligned thermoplastic polyurethane (TPU) was obtained by electrospinning mixed solvent with TPU granules (21 wt %) in DMF/ tetrahydrofuran (THF, volume ratio=1:1) on the collection device at a rotation speed of about 1200 rpm, a voltage of 26 kV, and a vertical reception distance of 20 cm (Fig. 3a).[55] These studies highlight the significant variation in optimal rotational speeds (1200-2000 rpm) across different polymer systems. This variability suggests the need for a comprehensive theoretical model that accounts for jet kinematics and whipping dynamics, polymer-specific viscoelastic properties and electrostatic field effects, mechanical drawing forces.

2.4.3 Coaxial electrospinning. The core-shell architecture is fabricated using coaxial electrospinning, where a specialized spinneret with concentric inner and outer tubes simultaneously delivers the core and shell precursor solutions. Two independent syringe pumps precisely control the injection rates of each solution.[56,57] Notably, coaxial electrospinning has emerged as an efficient and scalable approach for continuously fabricating these advanced core-shell fibrous materials with precise control over morphology and composition. Shin et al. developed 1 D cobalt-carbon core-shell nanofibers (Co-CSNFs) through a coaxial electrospinning approach, employing a dual-channel needle to simultaneously deliver a pure PAN solution (core, 0.3 mL min^{-1}) and a cobalt precursor/PAN mixture (shell, 0.5 mL min^{-1}) (Fig.3b).[58] The electrospinning process was conducted at 18 kV with a drum collector rotating at 1000 rpm, followed by direct heat treatment to obtain the final product without additional processing steps. Similarly, Liu et al. fabricated IrO_x@$SbSnO_x$ core-shell nanofiber catalysts using an advanced coaxial electrospinning system.[59] Their modified dual-channel nozzle design effectively separated the internal and external precursor solutions, ensuring precise core-shell formation. The process parameters included an applied voltage of 20 kV and a 15 cm working distance between the needle tip and the rotating collector.

The structural integrity and electrocatalytic performance of electrospun nanofibers are intrinsically determined by appropriate solution properties (*e.g.*, polymer molecular weight, viscosity, conductivity, surface tension), precise processing parameters (*e.g.*, applied voltage, solution flow rate, distance between spinneret and collector), stable environmental factors (*e.g.*, temperature, humidity), as well as ingenious spinneret and the collector design (*e.g.*, coaxial needle shape, collector geometry). Through systematic optimization of these parameters, electrocatalysts can be precisely engineered with tailored morphology and functional characteristics.

3. Advanced and efficient nanofibers for OER

Electrospun nanomaterials with high electrochemical activity and large surface areas are critically important for OER catalysis. Significant progress has been made in developing diverse electrospun catalysts, ranging from noble and non-noble metal oxides to metal sulfides, nitrides, carbons, conducting polymers and nanocomposites. To further enhance OER performance, advanced architectures, including tubular, porous, hierarchical, composite, and high-entropy structures, have been engineered through tailored fabrication and postprocessing strategies. This section provides a comprehensive overview of these advanced nanomaterials and their electrocatalytic properties.

3.1 Tubular structure

Nanotubes represent an exceptionally promising class of electrocatalytic materials due to their unique combination of structural and electronic properties. Their high surface area-to-volume ratio provides abundant active sites, significantly enhancing reaction kinetics and catalytic efficiency.[60,61] The inherent structural stability of nanotubes ensures robust mechanical and thermal performance during prolonged electrochemical operation. Furthermore, their excellent electrical conductivity facilitates efficient electron transfer throughout OER, minimizing energy barriers while maximizing reaction rates. These synergistic characteristics make nanotubes particularly well-suited for developing high-performance electrocatalysts in diverse energy conversion and storage systems.

Noble metal oxide-based catalysts represent the most promising class of transition metal oxide electrocatalysts for OER. A notable example is the binary Ru-Co mixed oxide nanotubes developed by Lee et al. through electrospinning.[62] The strategic substitution of Co into the rutile RuO_2 lattice and Ru into the spinel Co_3O_4 structure generated oxygen vacancies while incorporating Ru^{3+} into octahedral sites. The resulting $Ru_{0.47}Co_{0.53}O_y$ catalyst demonstrated decent performance, achieving an overpotential of 215 mV at 10 mA cm^{-2} and a Tafel slope of 40.1 mV dec^{-1} in 1.0 M $HClO_4$, along with enhanced stability compared to pure RuO_2. These improvements stem from the combined effects of the tubular morphology's high surface area, resistance to aggregation, and favorable structural transformations. Building on this success, Lee's group subsequently developed advanced architectures including $Cr_xIr_{1-x}O_2$ wire-in-tube alloys and IrO_2-ZnO multichannel nanotubes.[63,64] The Cr-rich oxide alloy (Cr:Ir = 62:38), synthesized via electrospinning and calcination, exhibited outstanding catalytic performance with an overpotential of 280 mV at 10 mA cm^{-2} and maintained stability for 24 hours in 1 M KOH.[64] Remarkably, the wire-in-

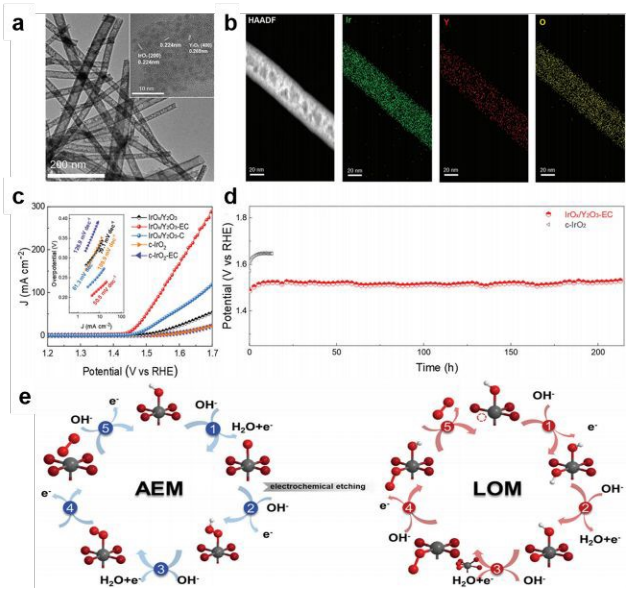

Fig. 4. (a) TEM image and high-resolution TEM (HRTEM) image of IrO_x/Y_2O_3-EC. (b) Elemental X-ray mapping images of IrO_x/Y_2O_3-EC. (c) Polarization curves and Tafel plots (inset) of the IrO_x/Y_2O_3-EC, IrO_x/Y_2O_3-C, as-synthesized IrO_x/Y_2O_3, c-IrO_2, and c-IrO_2-EC in 1.0 M KOH. (d) Galvanostatic stability of the OER at the current density of 10 mA cm^{-2} over IrO_x/Y_2O_3-EC in 1.0 M KOH. (e) Proposed OER mechanisms, including AEM (left) and LOM (right). The empty circle represents the oxygen vacancy. The gray, red, and white balls represent Ir, O, and H, respectively. Reproduced from ref. 65 with permission from John Wiley and Sons, copyright 2023.

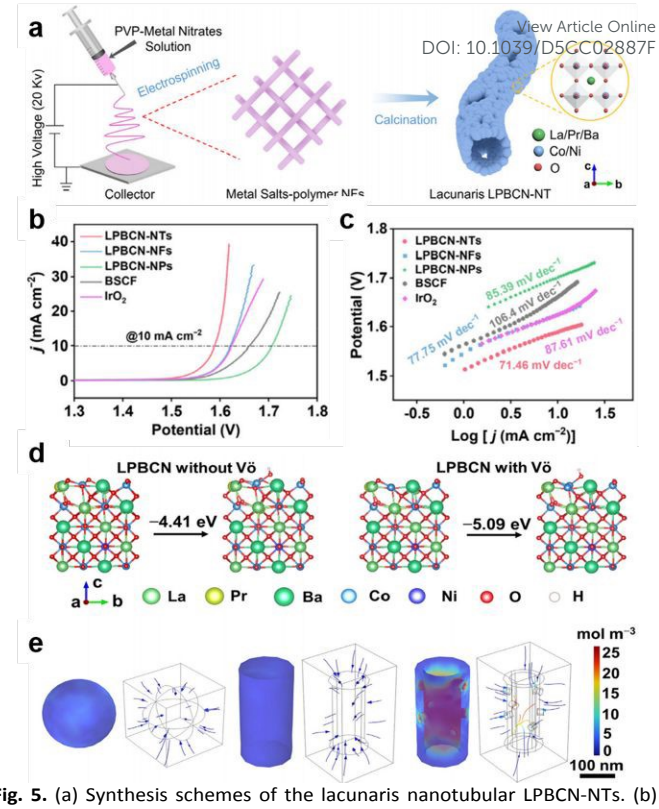

Fig. 5. (a) Synthesis schemes of the lacunaris nanotubular LPBCN-NTs. (b) The *iR*-corrected LSV curves and (c) the Tafel plots of all relevant electrocatalysts. (d) The DFT calculation results of OH^- adsorption energy over LPBCNs without and with oxygen vacancies, where Vö represents the oxygen vacancy. (e) The finite element analysis results of surface OH^- concentration and distribution over one NP, one NF and one lacunaris NT, respectively. Reproduced from ref. 68 with permission from RSC Publishing, copyright 2024.

tube $Cr_xIr_{1-x}O_2$@400°C displayed a double-layer capacitance 1.95-9.44 times greater than comparative samples, indicating significantly larger electroactive surface areas. The partial density of states (PDOS) analysis revealed that the d-band centers shifted closer to the Fermi level with the hybridized conduction band, therefore confirming the strong electronic interaction between Cr and Ir in the Cr-enriched catalyst ($Cr_{0.6}Ir_{0.4}O_2$). The increased DOS around the Fermi level implied enhanced conductivity of $Cr_{0.6}Ir_{0.4}O_2$ with superior OER activity. Density functional theory (DFT) calculations further demonstrated its lower OER overpotential than those of the comparative catalyst of IrO_2 and Cr_2O_3 on both the (110) and (211) surfaces. This improvement was attributed to the Cr-enriched composition for the optimized adsorption of *OOH species and the reduced Gibbs free energy barrier for OER.

To elucidate structure-activity-mechanism relationships in tubular catalysts, we developed IrO_x/Y_2O_3 nanotubes (Ir:Y = 6:4) with ≈20 nm inner diameters through electrospinning followed by calcination at 650°C (Fig. 4a-b).[65] The electrochemically acid-etched IrO_x/Y_2O_3-EC nanotubes exhibited exceptional OER performance, achieving a low overpotential of 223 mV at 10 mA cm^{-2} and remarkable stability exceeding 200 hours in 1 M KOH (Fig. 4c-d). Comprehensive characterization through pH-dependent studies, oxygen ion diffusion analysis, tetramethylammonium ion (TMA^+) detection, and differential electrochemical mass spectrometry (DEMS) revealed that the acidic etching treatment induced abundant oxygen vacancies and activated lattice oxygen sites, shifting the reaction mechanism from adsorbate evolution mechanism (AEM) to predominantly follow the lattice oxygen-mediated (LOM) pathway (Fig. 4e).

Recent advances in electrospun non-noble metal oxide catalysts have demonstrated exceptional alkaline OER performance through innovative structural and compositional design. Zhao et al. developed Co_3O_4/Bi_2MoO_6 heterojunction nanotubes that achieve a lower overpotential of 332 mV at 10 mA cm^{-2} and an optimized stability compared to individual components, with DFT studies revealing enhanced charge transfer across the interfacial electric field.[66] Further progress has been made with hierarchical Fe(III)/NiS nanotube systems, where the unique hollow architecture with vertically aligned nanosheets facilitates mass/electron transport and reconstructs into active Ni(Fe)OOH species during operation, yielding an impressive 264 mV overpotential and >70 h stability.[67] Notably, lacunaris perovskite nanotubes ($La_{0.5}Pr_{0.25}Ba_{0.25}Co_{0.8}Ni_{0.2}O_{3-\delta}$, LPBCN-NTs) synthesized via electrospinning and annealing exhibited an overpotential of 358.8 mV with a favorable Tafel slope of 71.46 mV dec^{-1} (Fig. 5a-c).[68] DFT calculations revealed that the adsorption energy of OH^- on the (110) plane of LPBCN with surface oxygen vacancies was −5.09 eV, significantly lower than that of the vacancy-free surface (−4.41 eV). This indicates a much stronger OH^- binding affinity induced by oxygen defects. Therefore, the lacunaris nanotubular structure exhibited an order of magnitude higher local OH^- concentration at the inner surface and pores as compared to the solid nanofibers and nanoparticles, accelerating OER kinetics. Moreover, the

abundant oxygen vacancies on LPBCN-NTs not only enhanced OH^- adsorption but also facilitated subsequent formation of *O intermediates, ultimately boosting their OER catalytic activity (Fig. 5d-e).

3.2 Porous structure

Porous architectures offer distinct advantages for OER electrocatalysts by simultaneously addressing three critical performance factors: (1) dramatically increased surface area that maximizes active site density, (2) enhanced mass transport of reactants (H_2O, OH^-) through interconnected pore networks, and (3) improved charge transfer efficiency.[69,70] These synergistic effects collectively boost both catalytic activity (particularly at high current densities) and reaction kinetics by minimizing diffusion limitations while maintaining structural integrity during prolonged operation.

Heteroatom-doped and porous carbon materials have emerged as promising metal-free OER electrocatalysts due to their cost-effectiveness, stability, and tunable electronic properties. Qiang et al. developed N-doped porous carbon nanofibers with optimized oxygen functionalities (NPCNFs-O) through electrospinning and carbonization, using β-cyclodextrin as a dual-function pore former and oxygen modulator (Fig. 6a-c).[71] The resulting NPCNFs-O exhibited a remarkably high surface area (723 $m^2\ g^{-1}$, 3.7 times greater than undoped NCNF) and hierarchical porosity (0.4-5 nm pores), enabling both abundant active sites and efficient mass transport (Fig. 6d-e). These structural advantages translated to excellent OER performance (η = 326 mV @ 10 mA cm^{-2}) and stability (Fig. 6f). In graphitic-N-doped carbon (NC), the carbon active sites exhibited a positive valence of +0.272. Through defect engineering, graphitic-N-doped defective carbon (NDC) increased this valence state to +0.326, while further carboxyl group functionalization in carboxyl-containing graphitic-N-doped defective carbon (ONDC) yielded the highest oxidation state of +0.328. This progressive charge enhancement can significantly strengthen the adsorption of negatively charged O_2 during OER. Based on the Gibbs free energy change (ΔG) of each elementary step in the OER process, the rate-determined step (RDS) of NC was the *O-to-*OOH transition, while the RDS of NDC and ONDC shifted to the *OH-to-*O step. Notably, the relatively lower ΔG to form *OOH intermediates in ONDC than that in NDC, identifying carboxyl groups as key active centers for charge density modulation and energy barrier reduction. Using biomass lignin as carbon precursor, PVP as spinning additive, zinc borate as boron source, ammonium fluoride as fluorine source and partial nitrogen source, B, N and F tri-doped lignin-based carbon porous nanofibers (BNF-LCFs) can be prepared by electrospinning and pyrolysis.[72] BNF-LCFs possessed a specific surface area of 981 $m^2\ g^{-1}$ and a smallest average pore size of 2.13 nm. Benefiting from the synergistic effect of B, N and F heteroatoms, large specific surface area and abundant defect sites, the BNF-LCF catalyst exhibited an overpotential of 342 mV at the current density of 10 mA cm^{-2} and a Tafel slope of 63.6 mV dec^{-1}.

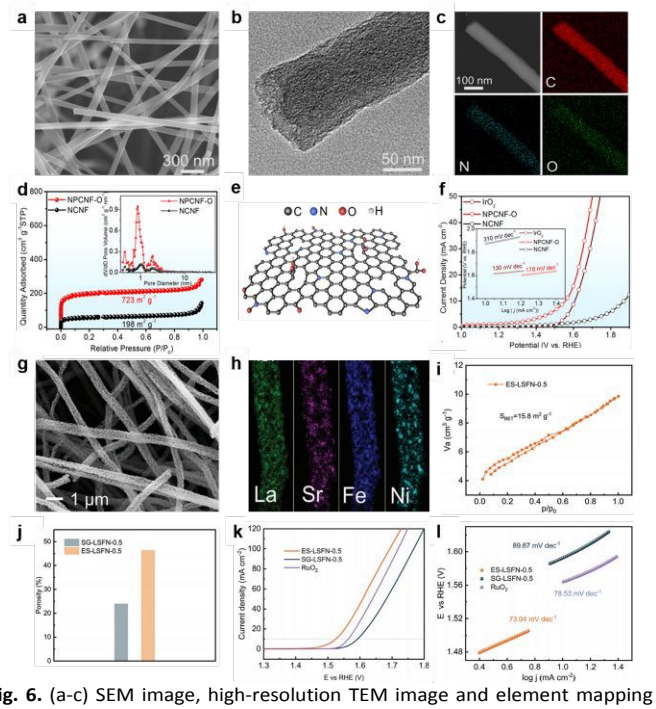

Fig. 6. (a-c) SEM image, high-resolution TEM image and element mapping images of NPCNF-O, respectively. (d) N_2 adsorption-desorption isotherms of NCNF and NPCNF-O, with the inset showing their corresponding pore size distribution curves. (e) Model structure for N,O codoped graphene. (f) OER LSV curves of NPCNF-O, NCNF, and IrO_2, with the inset showing the corresponding Tafel plots. Reproduced from ref. 71 with permission from American Chemical Society, copyright 2022. (g) SEM image of the ES-LSFN-0.5 nanofibers. (h) EDS mappings of the metal elements from ES-LSFN-0.5. (i) The nitrogen adsorption-desorption isotherm profiles of ES-LSFN-0.5. (j) The porosity values of ES-LSFN-0.5 and SG-LSFN-0.5 samples. (k) Polarization curves and (l) Tafel plots of the ES-LSFN-0.5, SG-LSFN-0.5, and RuO_2 electrocatalysts. Reproduced from ref. 75 with permission from John Wiley and Sons, copyright 2023.

Earth-abundant transition metal-based porous materials have emerged as highly efficient electrocatalysts for OER, combining exceptional activity with long-term stability in alkaline environments. Kundu et al. developed a hydrated cobalt phosphate fibrous network through electrospinning, achieving outstanding overpotentials of 245 mV in 1 M KOH and 457 mV in phosphate buffer at 10 mA cm^{-2}, where the interconnected porous structure facilitated rapid electron transfer and mass transport.[73] Significant progress has also been made in porous mixed-valence oxide systems, particularly spinel and perovskite structures. Sohn et al. synthesized Cr-substituted nickel ferrite ($NiCrFeO_4$) inverse spinel hollow nanofibers via electrospinning, where the Cr precursor promoted the formation of a high-surface-area porous architecture.[74] This unique structure delivered an overpotential of 298 mV with a low Tafel slope of 44.7 mV dec^{-1}, attributed to abundant active sites and optimized charge transfer. Similarly, Li et al. engineered nickel-doped $La_{0.5}Sr_{0.5}FeO_{3-\delta}$ (ES-LSFN-x) perovskite nanofibers with exceptional textural properties, 15.8 $m^2\ g^{-1}$ surface area and 46.4% porosity, far surpassing sol-gel-derived counterparts.[75] The porous and nanofibrous morphology not only achieved a low overpotential of 295 mV but also maintained 100-hour operational stability through the accelerated oxygen bubble release during OER. The oxygen vacancy formation energy (E_{ovf}) obtained from DFT calculations illustrated that ES-LSFN-0.5 exhibited an E_{ovf} of 1.56 eV, which was much lower than the

ES-LSFN-0 (2.08 eV), ES-LSFN-0.1 (2.04 eV), and ES-LSFN-0.3 (1.78 eV). This reduced E_{ovf} directly correlates with enhanced oxygen vacancy generation capacity induced by strategic Ni substitution. Moreover, with the narrowest p band gap (−2.48 eV) to Fermi level, ES-LSFN-0.5 was anticipated to be more conducive to enhance the OER activity, consistent with its lowest energy barrier of the *OOH-to-*O transition (0.45 eV).

3.3 Hierarchical structure

Hierarchical structures, which are characterized by multiscale architectures that integrate nanoscale features within larger micro- or macroscale frameworks, offer distinct advantages for electrocatalytic OER.[76,77] Their interconnected networks facilitate efficient electron and ion transport while maintaining robust structural integrity, enabling enhanced stability under harsh operational conditions, including mechanical stress and corrosive environments. These synergistic properties make hierarchical designs particularly effective for optimizing both the activity and durability of OER electrocatalysts.

Recent breakthroughs in electrospun hierarchical materials have significantly advanced the development of high-performance OER catalysts. The integration of transition metal phosphides within heteroatom-doped carbon matrices has proven particularly effective, as demonstrated by the Fe_2P/Co_2P heterojunction supported on N,P-codoped porous carbon.[77] This system achieves exceptional catalytic efficiency (320 mV overpotential at 10 mA cm^{-2} and a Tafel slope of 40.4 mV dec^{-1}) due to optimized electronic coupling and a conductive porous framework. Further performance enhancement was realized through hierarchical Co_3W_3C/CoP nanoparticles embedded in N,P-doped carbon fibers (CoWCP-NPC-2:1), where interfacial synergy and hierarchical engineering yielded a low 200 mV overpotential at 10 mA cm^{-2}.[78] A particularly innovative approach combines electrospinning with electrodeposition to create core-sheath architectures, exemplified by cobalt-carbon nanofibers uniformly coated with amorphous NiFeS nanosheets (Co-C/Ni_1Fe_1S). (Fig. 7a-c).[79] This design merges together the high conductivity of the carbonized core, the abundant active sites of the sulfide shell and impregnable structural stability, resulting in decent catalytic performance (an overpotential of 233 mV at 10 mA cm^{-2} and a Tafel slope of 53.1 mV dec^{-1}) and durability (54 h) in 1 M KOH (Fig. 7d-f).

A "carbon nanotube bridge" architecture was developed by integrating electrospinning, metal-organic framework (MOF) *in situ* growth, and carbonization, creating interconnected conductive pathways between cobalt-embedded carbon nanofibers.[80] This unique design achieves triple functionality: (1) optimizing the reaction microenvironment for enhanced oxygen adsorption kinetics, (2) enabling directional electron transport through shortened conduction paths, and (3) stabilizing the structure *via* π-π bond electron delocalization, collectively yielding a 380 mV overpotential at 10 mA cm^{-2} and a Tafel slope of 78 mV dec^{-1}. Further advancement was realized through a MOF/ covalent organic framework (COF) hybridization approach, where electrospinning combined with pyrolysis produced a 3D open framework (CNFs/CoZn- MOF@

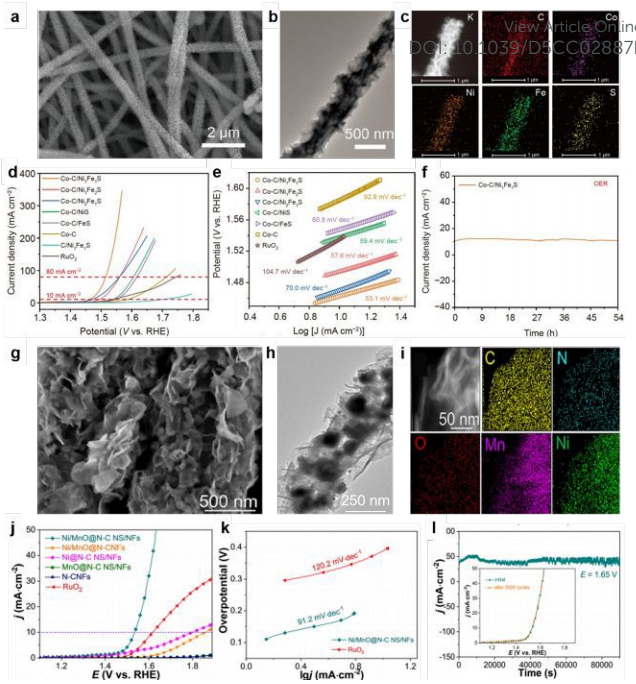

Fig. 7. (a, b) SEM and TEM images of Co-C/Ni_1Fe_1S nanofibers. (c) High-angle annular dark-field scanning transmission electron microscopy (HAADF- STEM) image and the corresponding elemental mapping images of C, Co, Ni, Fe and S for Co-C/Ni_1Fe_1S nanofibers. (d, e) LSV curves and Tafel plots of Co-C/Ni_1Fe_1S nanofibers and other catalysts for OER in 1M KOH solution with a scan rate of 1 mV s^{-1}. (f) The i-t curve of Co-C/Ni_1Fe_1S nanofibers at a potential of 0.56 V vs. Hg/HgO electrode. Reproduced from ref. 79 with permission from Springer Nature, copyright 2023. (g) SEM image, (h) HRTEM image and (i) EDS results of Ni/MnO@N-C NS/NFs. (j) LSV polarization curves of Ni/MnO@N-C NS/NFs, Ni/MnO@N-CNFs, Ni@N-C NS/NFs, MnO@N-C NS/NFs, N-CNFs, and RuO_2. (k) Tafel plots of Ni/MnO@N-C NS/NFs and RuO_2. (l) Chronoamperometric responses at 1.65 V, and inset is the LSV polarization curves of the Ni/MnO@N-C NS/NFs before and after 3000 cycles. Reproduced from ref. 82 with permission from Springer Nature, copyright 2025.

COF) featuring hierarchical porosity and high-density active sites.[81] The branch-leaf nanostructure, incorporating uniform Co nanoparticles and metal-N_x coordination sites, leverages synergistic effects between multiple active centers for superior catalytic performance. A particularly effective Ni/MnO heterostructure system was developed through electrospinning-pyrolysis-etching, where firmly anchored nanosheets/nanoparticles on N-doped carbon nanofibers create abundant interfaces (Fig. 7g-i).[82] Alkali etching introduced oxygen vacancies that optimally tune the electronic configuration, reducing the energy barrier for oxygen intermediate adsorption. This combined structural and electronic optimization results in exceptional activity (306 mV overpotential to attain 10 mA·cm^{-2}) while maintaining efficient mass transport through the open nanofiber network (Fig. 7j-l).

3.4 Composite structure

Composite electrocatalysts integrate diverse material components, including metals, metal oxides, carbons, and conducting polymers, to create multifunctional architectures with enhanced OER performance. Beyond simply increasing active site density and conductivity, these hybrid systems exploit synergistic interfacial effects where the collective

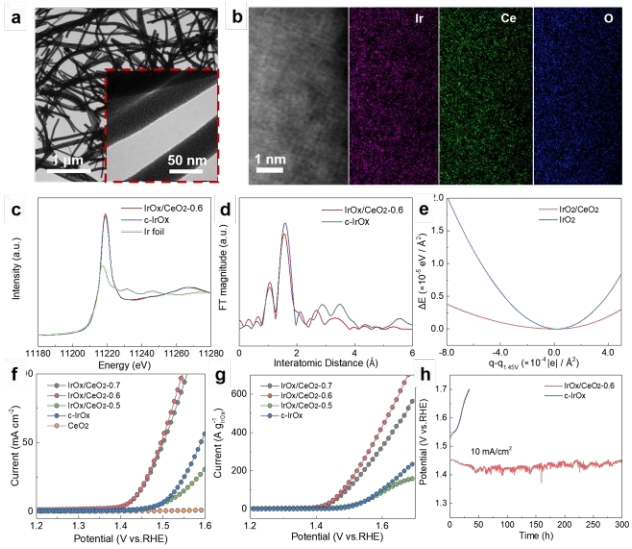

Fig. 8. (a) TEM images and (b) the elemental maps of IrO_x/CeO_2-0.6 nanowires. (c) Iridium L-edge XANES spectra and (d) EXAFS spectra for IrO_x/CeO_2-0.6 and c-IrO_x. (e) The energy cost for the electrode to hold or release extra charges. (f) LSV curves of various catalysts at a scanning rate of 10 mV s^{-1} in 0.5 M H_2SO_4. (g) LSV curves of various catalysts normalized by unit mass of iridium oxide. (h) Chronopotentiometry tests of IrO_x/CeO_2-0.6 and c-IrO_x at 10 mA cm^{-2}. Reproduced from ref. 85 with permission from Elsevier, copyright 2022.

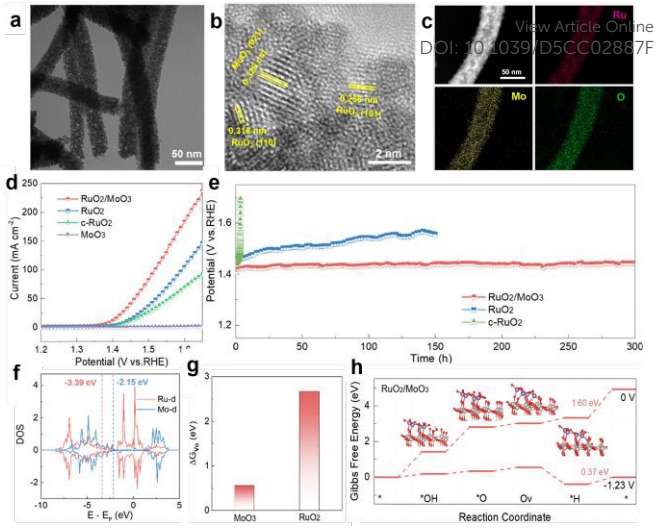

Fig. 9. (a, b) TEM image and HRTEM image of RuO_2/MoO_3. (c) Elemental mapping images of Ru (red), Mo (yellow), and O (green) in RuO_2/MoO_3. (d) LSV curves of RuO_2/MoO_3, RuO_2, c-RuO_2, and MoO_3 n 0.5 M H_2SO_4 solution. (e) Chronopotentiometry tests of RuO_2/MoO_3, RuO_2, and c-RuO_2. (f) DOS plots of Ru d and Mo d states in RuO_2/MoO_3. The dashed lines mean the d-band centres. (e) The calculated energy for the formation of oxygen vacancy in the respective RuO_2 and MoO_3 of the RuO_2/MoO_3 heterojunction. (h) The calculated energy barrier diagram of RuO_2/MoO_3. Reproduced from ref. 86 with permission from RSC Publishing, copyright 2024.

performance surpasses individual component contributions.[83,84] Critically, the heterointerfaces between constituent materials enable precise modulation of key properties: electronic structure for optimized intermediate adsorption, nanoscale morphology for improved ion transport, and surface chemistry for enhanced reaction kinetics. This interfacial engineering approach provides unparalleled opportunities for tailoring electrocatalytic activity and stability.

Our work has established new paradigms in the design of noble metal oxide composites for the challenging acidic OER, revealing critical atomic-scale mechanisms that govern both activity and stability. Through innovative electrospinning/calcination approaches, we developed amorphous and binary iridium oxide and ceria (IrO_x/CeO_2) composite nanowires that achieve breakthrough performance, 220 mV overpotential at 10 mA cm^{-2}, mass activity of 167 A g_{Ir}^{-1} at 1.51 V, and remarkable 300-hour stability in acidic media, far surpassing commercial IrO_x benchmarks [85] DFT calculations illustrated that IrO_2/CeO_2 could hold or release electrons at the cost of a smaller energy increment compared to pristine IrO_2. (Fig. 8). Comprehensive experimental characterizations and theoretical analysis demonstrated that CeO_2 served as an electron buffer at the nanoscale interface, modulating oxygen intermediate adsorption, lowering activation barriers (from 0.43 V to 0.28 V), and stabilizing Ir oxidation states. The CeO_2 component further inhibited the Ir dissolution under operational conditions by maintaining optimal electronic configurations, thereby synergistically improving both catalytic activity and long-term OER stability. Furthermore, we designed ruthenium and molybdenum oxide (RuO_2/MoO_3) composite nanowires with abundant and intimate interfaces by similar electrospinning/calcination process (Fig. 9a-c).[86] The RuO_2/MoO_3 composite catalysts exhibited a significantly low overpotential of 167 mV at 10 mA cm^{-2} and negligible degradation of OER performance in 0.5 M H_2SO_4 over 300 h (Fig. 9d-e). Extensively experimental evidences (*in situ* Raman, cyclic voltammetry analysis, *operando* Fourier transform infrared spectroscopy, *etc.*) and theoretical calculations demonstrated the occurrence of oxygen spillover from RuO_2 to MoO_3 and the subsequent participation of lattice oxygen of MoO_3 instead of RuO_2 for the steps of the release of oxygen, generation of oxygen vacancy and rehabilitation of lattice oxygen during acidic OER. By theoretically profiling the d-band center and formation energy of oxygen vacancy on RuO_2 and MoO_3, the spillover of reactive oxygen intermediate *O from RuO_2 to MoO_3 was feasible to suppresses the over-oxidation of ruthenium species of RuO_2 during acidic OER. Extensively experimental evidences and theoretical calculations verified the occurrence of oxygen spillover from RuO_2 to MoO_3 and the subsequent participation of lattice oxygen of MoO_3 instead of RuO_2 for the steps of the release of oxygen, leading to the enhanced activity and stability (Fig. 9f-h).

Recent advances in non-noble metal composite catalysts have achieved breakthrough performance in alkaline oxygen evolution, rivaling noble metal benchmarks while offering enhanced cost-effectiveness and durability. The CoP/FeOOH porous nanofiber system, fabricated through electrospinning followed by oxidation/phosphorization and FeOOH deposition, exhibits an overpotential of 250 mV to offer 10 mA cm^{-2}, a Tafel slope of 56.6 mV dec^{-1}, and a 20 h long-term test.[87] This performance stems from synergistic effects: FeOOH decoration optimizes oxygen intermediate adsorption, while the porous nanofiber architecture ensures abundant active sites, efficient electron transfer and gas bubble release. A more complex of FeS_2-Ni_3S_2 heterostructures and

$FeNi_3$ nanoparticles embedded within porous S, N co-doped carbon nanofibers (FeS_2-Ni_3S_2/$FeNi_3$@SN-CNF) demonstrates how *in situ* electrospinning can create multifunctional active centers.[88] The composite's 270 mV overpotential and 50 h stability originate from *in situ*-formed FeOOH/ $Ni(OH)_2$ active phases identified by *operando* Raman, $FeNi_3$ nanoparticles enhancing conductivity, and S,N-co-doping improving catalyst-support interaction. Utilizing chemical crosslinking electrospinning combined with carbonization, Mo_2C nanoparticles coupled with Ni can be *in situ* embedded into a N-doped porous carbon nanofiber network with frogspawn morphology.[89] Mo_2C/NCNTs@Ni delivered an overpotential of 320 mV at 10 mA cm^{-2} and a continuous operation test under different currents for 50 h in alkaline electrolyte due to the synergistic impact between Ni and Mo_2C nanoparticles and the conductive network.

3.5 High-entropy structure

High-entropy materials, defined by their single-phase solid solutions incorporating five or more principal elements, derive exceptional stability from high configurational entropy. These systems exhibit unique catalytic advantages, including multiple active metal centers, unsaturated coordination sites, and entropy-driven stabilization, which collectively enhance adsorption energetics, electron transfer kinetics, and operational durability.[90,91] As a transformative development in electrocatalysis, high-entropy architectures benefit significantly from electrospinning synthesis, which is a versatile approach that enables precise control over nanofiber composition, morphology, and scalability while maintaining phase purity. Recent advances in electrospun high-entropy alloys (HEA) and high-entropy oxides (HEO) have demonstrated their exceptional potential as OER electrocatalysts.

HEA electrocatalysts incorporating ruthenium and iridium precious metals were successfully synthesized through electrospinning, demonstrating exceptional performance for OER. Ultra-small FeCoNiIrRu HEA nanoparticles within carbon nanofibers (FeCoNiIrRu/CNF) were synthesized through this approach, exhibiting exceptional OER performance with a low overpotential of 241 mV at 10 mA cm^{-2} and a high mass activity of 205 mA mg^{-1}_{Ir+Ru}.[92] The catalytic performance of FeCoNiIrRu/CNF could be systematically tuned by modulating metal compositions and calcination temperatures. Theoretical calculations indicated electron density redistribution within the FeCoNiIrRu NPs, flowing from lower electronegativity elements (Fe, Co, Ni) to higher electronegativity elements (Ir, Ru), which enhanced the intrinsic activity of Ir sites and facilitated simultaneous promotion of *OOH intermediate conversion and O_2 generation. Additionally, the inherent hysteretic diffusion effect of HEA strongly inhibited metal leaching and dissolution, significantly improving operational durability. Utilizing a synergistic electrospinning, activation, and carbonization approach, a HEA electrocatalyst with high-temperature-carbonization (HCB) exhibited a high specific surface area of 1014 m^2 g^{-1} and mesoporous and microporous features.[93] The optimal FeCoNiMnRu-$HCB_{0.5}$ electrocatalyst

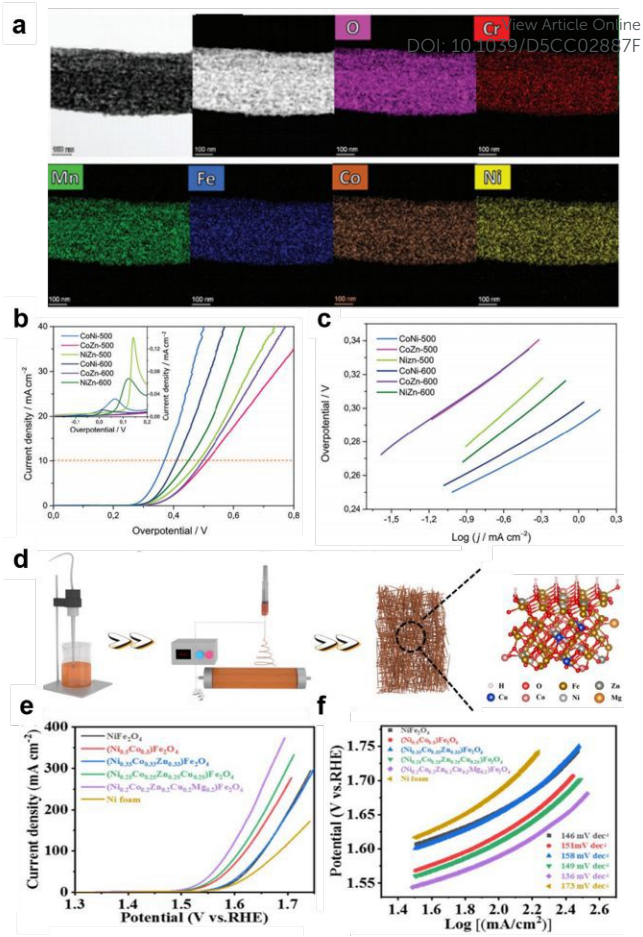

Fig. 10. (a) HAADF-STEM images of CoNi-500, followed by the elemental maps. (b) LSV curves recorded at a scan rate of 5 mV s^{-1} in 1.0 M KOH (pH≈13.8) for different HESO samples as electrocatalysts. (c) The corresponding Tafel curves. Reproduced from ref. 94 with permission from John Wiley and Sons, copyright 2023. (d) Synthesis schemes of $(Ni_{0.2}Co_{0.2}Zn_{0.2}Cu_{0.2}Mg_{0.2})Fe_2O_4$ spinel nanofibers. (e) IR-corrected LSV curves at 5 mV s^{-1} and (f) Tafel plots of $(Ni_{0.2}Co_{0.2}Zn_{0.2}Cu_{0.2}Mg_{0.2})Fe_2O_4$, $(Ni_{0.25}Co_{0.25}Zn_{0.25}Cu_{0.25})Fe_2O_4$, $(Ni_{0.33}Co_{0.33}Zn_{0.33})Fe_2O_4$, $(Ni_{0.5}Co_{0.5})Fe_2O_4$, $NiFe_2O_4$ and Ni foam in 1 M KOH electrolyte. Reproduced from ref. 97 with permission from RSC Publishing, copyright 2025.

demonstrated an overpotential of 229 mV at 10 mA cm^{-2} and a stability of 20 h. These findings establish this HEA-based electrocatalyst as a highly efficient and durable candidate for next-generation water splitting in alkaline media.

High-entropy spinel oxides (HESO) with multiple cheap transition metal cation sites offer a promising platform for the rational design of octahedral redox-active sites, thereby significantly enhancing intrinsic catalytic reactivity. The Cr/Mn/Fe/Co/Ni/Zn-based HESO nanofibers with granular architectures and oxygen-deficient surfaces were synthesized through electrospinning and low-temperature calcination (Fig. 10a).[94] The optimized CoNi-500 catalyst exhibited showed an overpotential of 360 mV at 10 mA cm^{-2} and a Tafel slope of 41 mV dec^{-1}, attributed to its tailored electronic structure, including lower outer 3d-electron configuration, optimal e_g orbital filling, and higher redox-active species distribution at 16 d sites (Fig. 10b-c). By precisely tuning the HESO composition, researchers achieved systematic control over fiber morphology,

View Article Online
DOI: 10.1039/D5CC02887F

Table 1. Summary of representative electrospun electrocatalysts toward OER.

Catalyst	Electrolyte	η_{10} (mV)	Tafel slope (mV dec^{-1})	Stability (h)	References
$Cr_xIr_{1-x}O_2$@400℃	1 M KOH	280	39.3	24	[64]
IrO_x/Y_2O_3-EC	1 M KOH	223	50.5	200	[65]
LPBCN-NTs	0.1 M KOH	358.8	71.46	8	[68]
NPCNFs-O	0.1 M KOH	326	178	-	[71]
BNF-LCFs	0.1 M KOH	342	63.6	-	[72]
ES-LSFN-0.5	1 M KOH	295	73.04	100	[75]
CoWCP-NPC-2:1	1 M KOH	200	72.0	10	[78]
Ni/MnO@N-C NS/NFs	0.1 M KOH	306	91.2	25	[82]
IrO_x/CeO_2-0.6	0.5 M H_2SO_4	220	63	300	[85]
RuO_2/MoO_3	0.5 M H_2SO_4	167	65	300	[86]
CoP/FeOOH	1 M KOH	250	56.6	20	[87]
$Ni_3S_2/FeNi_3$@SN-CNF	1 M KOH	270	-	50	[88]
FeCoNiIrRu/CNFs	0.5 M H_2SO_4	241	153	14	[92]
CoNi-500	1 M KOH	360	41	-	[94]
S400/2	1 M KOH	325	40	-	[96]
$(Ni_{0.2}Co_{0.2}Zn_{0.2}Cu_{0.2}Mg_{0.2})Fe_2O_4$	1 M KOH	286	136	200	[97]
S/LMO-E	1 M KOH	314	47	20	[98]
c-IrO_2	1 M KOH	471	109.9	20	[65]
c-RuO_2	0.1 M $HClO_4$	330	60.7	10	[99]

crystallinity, spinel inversion degree, oxygen vacancy concentration, and cation distribution, enabling fine-tuning of electrochemical properties. Further innovation came with the synthesis of $(FeCoNiCrMn)_3O_4$ nanofibers via electrospinning followed by quenching.[95] This approach modulated electron spin states through crystal-field effects, enhancing ferromagnetic properties. Applying an external magnetic field (~130 mT) further amplified spin-polarized electron transfer, weakening O-O bonds via spin-selective interactions and significantly reducing kinetic barriers. The morphology, crystallinity, defect density, and cation distribution within the lattice of (Cr, Mn, Fe, Co, Ni) HESO NF were further modulated by systematically varying calcination temperatures (300~800 °C) and duration (2h or 4 h).[96] The NFs calcined at 400 °C for 2 h delivered exceptional OER performance, achieving an overpotential of 325 mV and a Tafel slope of 40 mV dec^{-1} at 10 mA cm^{-2}. Broadband electrical spectroscopy revealed that the high oxygen vacancy mobility within the best-performing electrocatalyst correlated with very fast local dielectric relaxations of metal-coordination octahedra, experimentally confirming the essential roles of oxygen-deficient octahedral geometries. Another progress was achieved with $(Ni_{0.2}Co_{0.2}Zn_{0.2}Cu_{0.2}Mg_{0.2})Fe_2O_4$ spinel nanofibers, which showed decent activity (286 mV overpotential and 136 mV dec^{-1} Tafel slope) and remarkable 200-hour stability (Fig. 10d-f).[97] *Operando* studies revealed that the high-entropy structure promotes dynamic self-reconstruction during OER, generating oxygen vacancies while shifting the d-band center toward the Fermi level, an electronic configuration that optimally lowers the reaction energy barrier (ΔG_{max}).

High-entropy perovskite oxides (HEPOs) incorporating oxygen vacancies also demonstrate significant promises as efficient electrocatalysts for OER. A two-step synthetic method combining electrospinning and sulfurization was employed to introduce sulfur (S) dopant into HEPO containing La, Fe, Co, Ni, Cr, Mg elements.[98] This approach optimized the e_g orbital filling, while simultaneously increasing the active area, oxygen vacancy concentration, and electrical conductivity. Consequently, the resultant S-doped HEPO electrocatalyst delivered high OER performance, achieving an overpotential of 314 mV at 10 mA cm^{-2} and a Tafel slope of 47 mV dec^{-1} with faster kinetics, alongside a stability of 20 h. Mechanistic studies confirmed LOM participation, supported by pronounced pH-dependent activity trends and selective inhibition in the presence of TMA^+.

Based on the above analysis, electrospinning has emerged as a highly promising technique for fabricating nanostructured OER electrocatalysts with diverse architectures including

tubular, porous, hierarchical, composite and high-entropy configurations (Table 1). These structures offer exceptional advantages such as large surface areas, abundant active sites, tunable composition, and efficient mass transport. However, translation of their impressive lab-scale performance into commercially viable, industrial-scale electrolyzers encounters two interconnected challenges: scalability of complex fiber architectures and long-term stability under harsh industrial operating conditions.[27] Reproducing fiber electrocatalysts with identical diameter, porosity, surface roughness, and complex features across large-area electrodes is extremely challenging. Variations in the properties of precursor solutions and synthetic parameters of electrospinning become amplified during continuous, large-scale operations. Minor fluctuations can lead to bead formation, fiber diameter inconsistencies, or loss of desired secondary structures. Laboratory stability tests often fail to be replicated using industrial electrolyzers with much higher current densities. These conditions generate intense local pH gradients, significant mechanical stress from oxygen bubble evolution, and pronounced Joule heating. Therefore, intensive efforts are still required to advance electrospinning technologies and develop innovatively engineered fiber architectures for OER.

4. Conclusions and outlook

Electrospinning technology has emerged as a highly versatile and scalable approach for the rational design and synthesis of advanced electrocatalysts for OER. By enabling precise control over the geometrical morphology, chemical composition, and electronic structure of catalysts, electrospinning offers a unique solution to address critical OER challenges, including sluggish kinetics, high overpotential, and inadequate stability. The 1D nanostructures produced by electrospinning, such as tubular, porous and hierarchical structures, provide high surface areas, enhanced mass transport, and improved electron transfer capability, which are critical for maximizing OER performance. Furthermore, the capability of electrospinning to incorporate multiple active components in one catalyst, such as hybrid composites and high-entropy metal oxides, allows the realization of synergistic catalytic effects that significantly boost both activity and stability.

Despite these advancements, several critical challenges remain to be addressed to fully realize the potentials of electrospun OER electrocatalysts for practical applications. Scalability and cost-effectiveness of electrocatalysts is the primary concern. Despite electrospinning is inherently scalable, the economic viability of large-scale production requires reductions in raw material costs and process complexity. Future research should focus on developing low-cost precursors and optimizing the electrospinning process to achieve high-throughput fabrication without compromising the quality of the electrocatalysts.

Electrospun electrocatalysts additionally serve as ideal model systems for fundamental mechanistic investigations, where their tunable nanostructures enable the elucidation of structure-activity relationships and the discovery of new catalytic pathways. These insights are invaluable for guiding the rational design of next-generation catalysts optimized for both performance and durability under practical operating conditions.

Advanced characterization methodologies will play a crucial role in understanding the structure-activity relationships of electrospun electrocatalysts.[99] *In situ* and *operando* characterization techniques, such as X-ray absorption spectroscopy (XAS), Raman spectroscopy, and liquid-phase electron microscopy, can provide unprecedented opportunities to monitor dynamic catalytic processes and structural evolution during OER. These insights establish the instructive principles for optimizing the design of electrospun electrocatalysts and tailoring their properties for promoted OER.

Importantly, the integration of electrospun electrocatalysts into functional energy devices represents a critical frontier. Although significant progress has been achieved in laboratory-scale studies, the performance and durability of these electrocatalysts under realistic operated devices, such as proton exchange membrane water electrolyzers (PEMWEs) and rechargeable metal-air batteries, needs to be rigorously evaluated. Device-level optimization, including the development of efficient electrode architectures, the minimization of interfacial resistances, and gas/liquid transport enhancement, will be decisive for achieving their high performance in commercial applications.

In conclusion, electrospinning technology provides a powerful and flexible platform for the design and synthesis of high-performance OER electrocatalysts. The unique advantages of electrospun materials, including their tunable morphology, high surface area, and compositional versatility, make them highly promising for addressing the challenges of OER in energy conversion and storage technologies. With continued advancements in electrocatalyst design, processing techniques, and device integration, coupled with interdisciplinary collaboration, electrospun electrocatalysts have the potential to play a pivotal role in the transition to a sustainable energy future.

Author contributions

This manuscript was collaboratively written by all authors. The final version of the manuscript has been approved by all authors.

Data availability statement

No primary research results, software or code have been included and no new data were generated or analysed as part of this review.

Conflicts of interest

There are no conflicts to declare.

View Article Online
DOI: 10.1039/D5CC02847F

Acknowledgements

This work was supported by Shaanxi Provincial Natural Science Basic Research Program Project (NO. 2025JC-YBMS-136) and Xihang Research Fund Project (NO.2024KY02342).

Notes and references

1 Q. Zhang, S. Dong, P. Shao, Y. Zhu, Z. Mu, D. Sheng, T. Zhang, X. Jiang, R. Shao, Z. Ren, J. Xie, X. Feng and B. Wang, *Science*, 2022, **378**, 181-186.
2 Š. Kment, A. Bakandritsos, I. Tantis, H. Kmentová, Y. Zuo, O. Henrotte, A. Naldoni, M. Otyepka, R. S. Varma and R. Zbořil, *Chem. Rev.*, 2024, **124**, 11767-11847.
3 S. Chandrasekaran, Q. Wang, Q. Liu, H. Wang, D. Qiu, H. Lu, Y. Liu, C. Bowen and H. Huang, *Chem. Soc. Rev.*, 2025, **54**, 2275-2343.
4 Q. Huang, B. Xia, M. Li, H. Guan, M. Antonietti and S. Chen, *Nat. Commun.*, 2024, **15**, 4157.
5 E. D. Helal, W. Xu, Y. Li, L. Gao, H. Sun, Q. Xu, I. A. Chandio, S. Abbas, A. H. Pato and W. Liu, *Chem. Commun.*, 2025, **61**, 10126-10129.
6 K. Yang, M. Li, T. Gao, G. Xu, D. Li, Y. Zheng, Q. Li and J. Duan, *Nat. Commun.*, 2024, **15**, 7060.
7 L. Chong, G. Gao, J. Wen, H. Li, H. Xu, Z. Green, J. D. Sugar, A. J. Kropf, W. Xu, X.-M. Lin, H. Xu, L.-W. Wang and D.-J. Liu, *Science*, 2023, **380**, 609-616.
8 W. Gou, Y. Wang, M. Zhang, X. Tan, Y. Ma and Y. Qu, *Chin. J. Catal.*, 2024, **60**, 68-106.
9 X. Yan, N. Liu, W. Liu, J. Zeng, C. Liu, S. Chen, Y. Yang, X. Gui, D. Yu, G. Yang and Z. Zeng, *Chem. Commun.*, 2024, **60**, 12787-12802.
10 L. Quan, H. Jiang, G. Mei, Y. Sun and B. You, *Chem. Rev.*, 2024, **124**, 3694-3812.
11 V.-H. Do and J.-M. Lee, *Chem. Soc. Rev.*, 2024, **53**, 2693-2737.
12 J. Li, Y. Ma, J. C. Ho and Y. Qu, *Acc. Chem. Res.*, 2024, **57**, 895-904.
13 W. Shi, T. Shen, C. Xing, K. Sun, Q. Yan, W. Niu, X. Yang, J. Li, C. Wei, R. Wang, S. Fu, Y. Yang, L. Xue, J. Chen, S. Cui, X. Hu, K. Xie, X. Xu, S. Duan, Y. Xu and B. Zhang, *Science*, 2025, **387**, 791-796.
14 H. Lei, W. Yang, S. Hu, L. Yi, C. Ma, C. Hu, F. Qian, M. Zhao, L. Liu, G. Yang and Q. Chen, *Angew. Chem. Int. Ed.*, 2025, e202503871.
15 L. C. Seitz, C. F. Dickens, K. Nishio, Y. Hikita, J. Montoya, A. Doyle, C. Kirk, A. Vojvodic, H. Y. Hwang, J. K. Norskov and T. F. Jaramillo, *Science*, 2016, **353**, 1011-1014.
16 J. Zhang, X. Fu, S. Kwon, K. Chen, X. Liu, J. Yang, H. Sun, Y. Wang, T. Uchiyama, Y. Uchimoto, S. Li, Y. Li, X. Fan, G. Chen, F. Xia, J. Wu, Y. Li, Q. Yue, L. Qiao, D. Su, H. Zhou, W. A Goddard and Y. Kang, *Science*, 2025, **387**, 48-55.
17 X. Wang, W. Pi, S. Hu, H. Bao, N. Yao and W. Luo, *Nano-Micro Lett.*, 2025, **17**, 11.
18 Y. Wang, P. Guo, J. Zhou, B. Bai, Y. Li, M. Li, P. Das, X. Wu, L. Zhang, Y. Cui, J. Xiao and Z.-S. Wu, *Energy Environ. Sci.*, 2024, **17**, 8820-8828.
19 J. Wang, X. Li, H. Liang, C. Zhang, H. Du, Y. Sun, H. Li, H. Pan, Y. Hao, M. Zhao, T. Li and T. Ma, *Adv. Funct. Mater.*, 2025, 2503596.
20 R. Mehmood, W. Fan, X. Hu, J. Li, P. Liu, Y. Zhang, Z. Zhou, J. Wang, M. Liu and F. Zhang, *J. Am. Chem. Soc.*, 2023, **145**, 12206-12213.
21 C. Luan, D. Escalera-López, U. Hagemann, A. Kostka, G. Laplanche, D. Wu, S. Cherevko and T. Li, *ACS Catal.*, 2024, **14**, 12704-12716.
22 R. Liu, M. Sun, X. Liu, Z. Lv, X. Yu, J. Wang, Y. Liu, L. Li, X. Feng, W. Yang, B. Huang and B. Wan, *Angew. Chem. Int. Ed.*, **2023**, 62, e202312644.
23 A. Thomas, A. Kumar, R. K. Sharma, E. C. Buck, B. Gwalani, M. Bhogra and H. S. Arora, *J. Mater. Chem. A*, 2024, **12**, 22832-22843.
24 S. Peng, G. Jin, L. Li, K. Li, M. Srinivasan, S. Ramakrishna and J. Chen, *Chem. Soc. Rev.*, 2016, **45**, 1225-1241.
25 D. Zhang, D. Wang, B. Feng, J. Cheng, H. Yan, J. Chang, Z. Wang, P. K. Chu and Y. Luo, *Chem. Commun.*, 2024, **60**, 7590-7593.
26 J. Xue, T. Wu, Y. Dai and Y. Xia, *Chem. Rev.*, 2019, **119**, 5298-5415.
27 Z. Wang, W. Fan, Z. Xue, C. Dong, J. Li, S. Jia, S. Zhou, X. Fang, Y. Yan and M. Liu, *Chem. Eng. J.*, 2025, **519**, 165352.
28 M. Li, Y. Liang, J. Shi, Q. Li, Q. Xu and W.-B. Cai, *Chem. Rec.*, 2025, **25**, e202400240.
29 Y. Liao, C.-H. Loh, M. Tian, R. Wang and A. G. Fane, *Prog. Polym. Sci.*, 2018, **77**, 69-94.
30 Z. Zhang, X. Wu, Z. Kou, N. Song, G. Nie, C. Wang, F. Verpoort and S. Mu, *Chem. Eng. J.*, 2022, **428**, 131133.
31 D. Zhang, D. Wang, B. Feng, J. Cheng, H. Yan, J. Chang, P. K. Chu and Y. Luo, *Inorg. Chem.*, 2024, **63**, 23858-23866.
32 H. Cao, B. Liu, J. Bai, C. Li and G. Xu, *J. Alloys Compd.*, 2025, **1010**, 178041.
33 Z. Wang, S. Han, Y. Zhang, X. Wang, Q. Bai and Y. Wang, *Renew. Energy*, 2024, **233**, 121180.
34 Z.-M. Huang, Y.-Z. Zhang, M. Kotaki and S. Ramakrishna, *Compos. Sci. Technol.*, 2003, **63**, 2223-2253.
35 D. Li and Y. Xia, *Adv. Mater.*, 2004, **16**, 1151-1170.
36 N. Bhardwaj and S. C. Kundu, *Biotechnol. Adv.*, 2010, **28**, 325-347.
37 C. Niu, J. Meng, X. Wang, C. Han, M. Yan, K. Zhao, X. Xu, W. Ren, Y. Zhao, L. Xu, Q. Zhang, D. Zhao and L. Mai, *Nat. Commun.*, 2015, **6**, 7402.
38 X. Zong, K. Kim, D. Fang, S. Ran, B. S. Hsiao and B. Chu, *Polymer*, 2002, **43**, 4403-4412.
39 S. V. Fridrikh, J. H. Yu, M. P. Brenner and G. C. Rutledge, *Phys. Rev. Lett.*, 2003, **90**, 144502.
40 S. Yang, X. Wang, B. Ding, J. Yu, J. Qian and G. Sun, *Nanoscale*, 2011, **3**, 564-568.
41 M. Inagaki, Y. Yang and F. Kang, *Adv. Mater.*, 2012, **24**, 2547-2566.
42 T. J. Sill and H. A. von Recum, *Biomaterials*, 2008, **29**, 1989-2006.
43 M. M. Demir, I. Yilgor, E. Yilgor and B. Erman, *Polymer*, 2002, **43**, 3303-3309.
44 G.-Z. Yang, H.-P. Li, J.-H. Yang, J. Wan and D.-G. Yu, *Nanoscale Res. Lett.*, 2017, **12**, 55.
45 P. K. Szewczyk and U. Stachewicz, *Adv. Colloid Interface Sci.*, 2020, **286**, 102315.
46 H. Zhao, B. Song, H. Li, X. Li, C. Ge, Q. Wu, J. Chen, Z. Wang, G. Yan and J. Fang, *Small*, 2025, **21**, 2407700.
47 M. Zhang, Y. Liu and C. Li, *Int. J. Hydrogen Energy*, 2023, **48**, 1107-1119.
48 L. He, X. Wang, T. Gao, W. Yang, Q. Jian, J. Liu, B. Li, Z. Wu and Y. Ruan, *J. Colloid Interface Sci.*, 2025, **693**, 137624.
49 B. Zhang, F. Kang, J.-M. Tarascon and J.-K. Kim, *Prog. Mater. Sci.*, 2016, **76**, 319-380.
50 M. Zhong, M. Xu, S. Ren, W. Li, C. Wang, M. Gao and X. Lu, *Energy Environ. Sci.*, 2024, **17**, 1984-1996.
51 W. Gou, M. Zhang, Y. Zou, X. Zhou and Y. Qu, *ChemCatChem*, 2019, **11**, 6008-6014.
52 Y. Cho, J. W. Beak, M. Sagong, S. Ahn, J. S. Nam and I.-D. Kim, *Adv. Mater.*, 2025, 2500162.
53 C. Shi, S. Yu and C. Li, *Chem. Eng. J.*, 2022, **441**, 136052.
54 Z. Zeng, T. Zhang, Y. Liu, W. Zhang, Z. Yin, Z. Ji and J. Wei, *ChemSusChem*, 2018, **11**, 580-588.

55 J. Li, Y. Zhao, W. Zhai, X. Zhao, K. Dai, C. Liu and C. Shen, *Chem. Eng. J.*, 2024, **485**, 149952.
56 Y. A. Alli, A. Bamisaye, A. T. Onawole, P. O. Oladoye, O. M. Bankole, B. Koivisto and K. Youssef, *Nano Energy*, 2024, **131**, 110203.
57 H. Qu, S. Wei and Z. Guo, *J. Mater. Chem. A*, 2013, **1**, 11513-11528.
58 S. Shin, Y. Yoon, S. Park and M. W. Shin, *J. Alloys Compd.*, 2023, **939**, 168731.
59 Z. Liu, Y. Lu, Z. Cui and R. Qi, *ACS Appl. Mater. Interfaces*, 2023, **15**, 10606-10620.
60 W. Peng, Y. Wang, X. Yang, L. Mao, J. Jin, S. Yang, K. Fu and G. Li, *Appl. Catal. B*, 2020, **268**, 118437.
61 L. Li, M. Yu, C. Gao, X. Yan, N. Zhang, J. Bao and X. Zhang, *J. Alloys Compd.*, 2024, **1003**, 175530.
62 A. Yu, M. H. Kim, C. Lee and Y. Lee, *Nanoscale*, 2021, **13**, 13776-13785.
63 Y. Nam, D. Jin, S. Choi, D. H. Hong, H. R. Moon and Y. Lee, *Appl. Surf. Sci.*, 2024, **644**, 158741.
64 D. Jin, J. Kang, S. Prabhakaran, Y. Lee, M. H. Kim, D. H. Kim and C. Lee, *J. Mater. Chem. A*, 2022, **10**, 13803-13813.
65 X. Tan, M. Zhang, D. Chen, W. Li, W. Gou, Y. Qu and Y. Ma, *Small*, 2023, **19**, 2303249.
66 X. Zhao, M. Liu, Z. Shang, Q. Lu, X. Han, X.-Y. Ji and H. Zhang, *Energy Fuels*, 2024, **38**, 17939-17947.
67 M. Zhong, W. Li, J. Chen, S. Ren, R. Qi, C. Wang and X. Lu, *Sep. Purif. Technol.*, 2023, **310**, 123164.
68 L.-B. Liu, S. Liu, Y.-F. Tang, Y. Sun, X.-Z. Fu, J.-L. Luo and S. Liu, *Nanoscale*, 2024, **16**, 16458-16466.
69 F. Zhang, Y. Si, J. Yu and B. Ding, *Chem. Eng. J.*, 2023, **456**, 140989.
70 X. Liu, P. Chen, W. Wang, W. Li, Y. Rao, Y. Wang, J. Zhao, L. Su n, W. Liu and Y. Cheng, *J. Alloys Compd.*, 2024, **979**, 173432.
71 F. Qiang, J. Feng, H. Wang, J. Yu, J. Shi, M. Huang, Z. Shi, S. Liu, P. Li and L. Dong, *ACS Catal.*, 2022, **12**, 4002-4015.
72 Y. Wang, R. Gan, S. Zhao, W. Ma, X. Zhang, Y. Song, C. Ma and J. Shi, *Appl. Surf. Sci.*, 2022, **598**, 153891.
73 S. S. Sankar, A. Rathishkumar, K. Geetha and S. Kundu, *Int. J. Hydrogen Energy*, 2021, **46**, 10366-10376.
74 P. Ramakrishnan, K. B. Lee, G.-J. Choi, I.-K. Park and J. I. Sohn, *J. Ind. Eng. Chem.*, 2021, **101**, 178-185.
75 L. Li, Z. Zheng, J. Li, Y. Mu, Y. Wang, Z. Huang, Y. Xiao, H. Huang, S. Wang, G. Chen and L. Zeng, *Small*, 2023, **19**, 2301261.
76 Y. Gao, S. Liang, C. Jiang, M. Gu, Q. Zhang, A. Abdelhafiz, Z. Zhang, Y. Han, Y. Yang, X. Zhang, P. Liang, J. Li and X. Huang, *Sci. Adv.*, 2025, **11**, eads7154.
77 K. Huang, J. Hu, J. Cao, X. Wei, S. Liu, Q. Dai, F. Shen, X. Zhang, X. Zhao, Y. Peng, Z. Deng and Y. Huang, *Sci China Chem.*, 2025, 68.
78 Y. Zhang, W. Shi, L. Bo, Y. Shen, X. Ji, L. Xia, X. Guan, Y. Wang and J. Tong, *Chem. Eng. J.*, 2022, **431**, 134188.
79 W. Li, M. Zhong, X. Chen, S. Ren, S. Yan, C. Wang and X. Lu, *Sci. China Mater.*, 2023, **66**, 2235-2245.
80 T. Lu, N. Xu, L. Guo, B. Zhou, L. Dai, W. Yang, G. Liu, J. K. Lee and J. Qiao, *Adv. Fiber Mater.*, 2024, **6**, 1108-1121.
81 L. Liu, Q. He, S. Dong, M. Wang, Y. Song, H. Diao and D. Yuan, *J. Colloid Interface Sci.*, 2024, **666**, 35-46.
82 C. Ge, Z.-J. Li, Y.-N. Chang, T.-F. Li, B. He, T.-Y. Lu and L. Xu, *Rare Met.*, 2025, **44**, 3107-3118.
83 H. Ge, J. Wang, Y. Luo, B. Shi, J. Jiang, S. Cui, L. Cheng, Z. Li and Z. Jiao, *Carbon*, 2024, **229**, 119482.
84 C. Xu, Y. Li, D. Li, Y. Zhang, B. Liu, M. D. H. Akhon and P. Huo, *Nanoscale*, 2024, **16**, 8286-8306.
85 W. Gou., Z. Xia, X. Tan, Q. Xue, F. Ye, S. Dai, M. Zhang, R. Si, Y. Zou, Y. Ma, J. C. Ho and Y. Qu, *Nano Energy*, 2022, **104**, 107960.
86 W. Gou, S. Zhang, Y. Wang, X. Tan, L. Liao, Z. Qi, M. Xie, Y. Ma, Y. Su and Y. Qu, *Energy Environ. Sci.*, 2024, **17**, 6755-6765.
87 J. Cheng, B. Shen, Y. Song, J. Liu, Q. Ye, M. Mao and Y. Cheng, *Chem. Eng. J.*, 2022, **428**, 131130.
88 Y. Li, W. Ma, J. Wang and Q. Zhong, *J. Mater. Chem. A*, 2022, **10**, 24388-24397.
89 Z. Wan, L. Wang, Y. Zhou, S. Xu, J. Zhang, X. Chen, S. Li, C. Ou and X. Kong, *Nanoscale*, 2024, **16**, 5845-5854.
90 Y. Chen, C. Chen, W.-H. Huang, C.-W. Pao, C.-C. Chang, T. Mao, J. Wang, H. Fu, F. Lai, N. Zhang and T. Liu, *ACS Nano*, 2024, **18**, 20530-20540.
91 C. Chen, Z. Xu, G. Hai, W.-H. Huang, C.-W. Pao, H. Li, K. Jiang, N. Zhang and T. Liu, *Small*, 2025, **21**, 2407964.
92 H. Zhu, Z. Zhu, J. Hao, S. Sun, S. Lu, C. Wang, P. Ma, W. Dong and M. Du, *Chem. Eng. J.*, 2022, **431**, 133251.
93 L. Wang, C. Wang, Y. Mu, J. Fan, X. Yang, C. Yu, B. Guo and G. Zeng, *Fuel*, 2025, **391**, 134800.
94 C. Triolo, K. Moulaee, A. Ponti, G. Pagot, V. D. Noto, N. Pinna, G. Neri and S. Santangelo, *Adv. Funct. Mater.*, 2024, **34**, 2306375.
95 Z. Gao, J.-H. Liu, S. Wang, W. Yang, W. Wang, L. Li, H. Guo, J. Zheng, S. Ramakrishna, J. Zhang, L. Yan and Y.-Z. Long, *Chem. Eng. J.*, 2024, **496**, 154216.
96 K. Vezzù, C. Triolo, K. Moulaee, G. Pagot, A. Ponti, N. Pinna, G. Neri, S. Santangelo, V. D. Noto, *Small*, 2025, **21**, 2408319.
97 M. Zhang, X. Zhou, K. Luo, Y. Fan, C. He, Q. Niu, J. Zhang, P. Zhang and S. Dai, *J. Mater. Chem. A*, 2025, **13**, 1287-1301.
98 Z. Wang, S. Han, Y. Zhang, X. Wang, Q. Bai and Y. Wang, *Renew. Energy*, 2024, **233**, 121180.
99 Z.-Y. Wu, F.-Y. Chen, B. Li, S.-W. Yu, Y. Z. Finfrock, D. M. Meira, Q.-Q. Yan, P. Zhu, M.-X. Chen, T.-W. Song, Z. Yin, H.-W. Liang, S. Zhang, G. Wang and H. Wang, *Nat. Mater.*, 2023, **22**, 100-108.
100 X. Zheng, S. Ding, Y. Li, J. Cai, J. Hao, Z. Zhuang, C. Wang, M. Du and H. Zhu, *Chem. Eng. J.*, 2025, **512**, 162508.

View Article Online
DOI: 10.1039/D5CC02887F

No primary research results, software or code have been included and no new data were generated or analysed as part of this review.